Electronic Supplementary Information

Redox-Active Conductive Metal-Organic Framework with High Lithium Capacities at Low Temperatures

Yogendra Kumar,[a‡] Tae Hyeong Kim,[b‡] Iyan Subiyanto,[ac] Winda Devina,[a] Segi Byun,[a] Subhajit Nandy,[d] Keun Hwa Chae,[d] Suim Lim,[e] Bumjin Kim,[b] Sanghui Kang,[b] Seong Ok Han,[a] Kanghoon Yim,*[e] Jungjoon Yoo*[b] and Hyunuk Kim*[ac]

[a] Hydrogen Convergence Materials Laboratory, Korea Institute of Energy Research (KIER), 152 Gajeong-ro, Yuseong-gu, Daejeon, 34129, Republic of Korea

[b] Energy Storage Laboratory, Korea Institute of Energy Research (KIER), 152 Gajeong-ro, Yuseong-gu, Daejeon, 34129, Republic of Korea

[c] Energy Engineering, University of Science and Technology (UST), 217 Gajeong-ro, Yuseong-gu, Daejeon, 34113, Republic of Korea

[d] Advanced Analysis Center, Korea Institute of Science and Technology (KIST), 5, Hwarang-ro 14-gil, Seongbuk-gu, Seoul, 02792, Republic of Korea

[e] Computational Science & Engineering Laboratory, Korea Institute of Energy Research (KIER), 152 Gajeong-ro, Yuseong-gu, Daejeon, 34129, Republic of Korea

‡ These authors contributed equally.
Correspondence should be addressed to K. Y. (khyim@kier.re.kr), J. Y. (jjyoo@kier.re.kr) and H.K. (hyunuk@kier.re.kr).
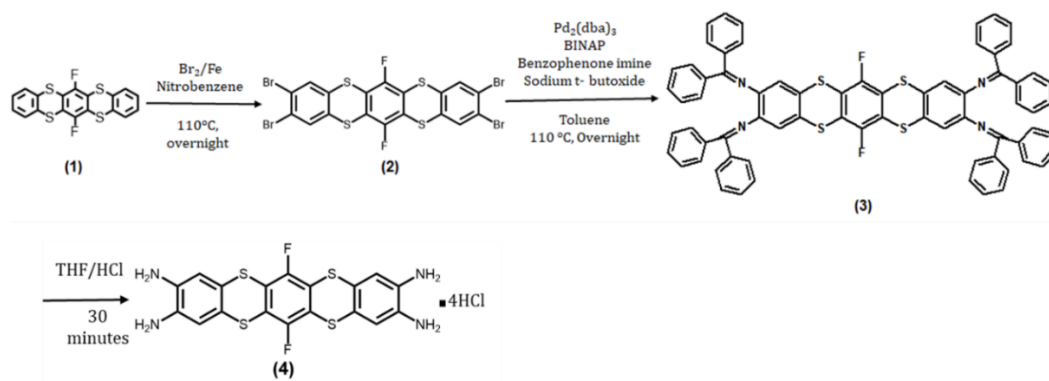
Figure S1. Synthetic scheme of 6,13-difluorobenzo[5,6][1,4]dithio[2,3-*b*]thianthrene-2,3,9,10-tetraamine (TATH) **(4)**

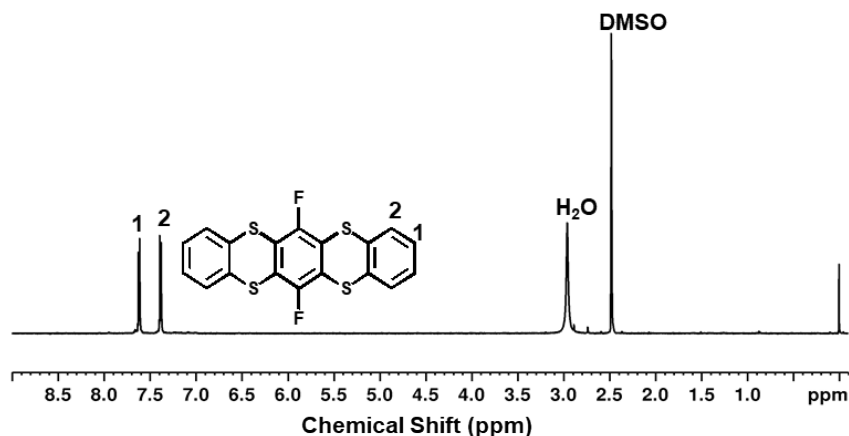**6,13-Difluorobenzo[5,6][1,4]dithiino[2,3-*b*]thianthrene (1)** was synthesized via reported procedure.[11]

Figure S2. ^{1}H NMR spectra of **(1)** in DMSO at 85 ^{o}C

2,3,9,10-TetraBromo-6,13-Difluorobenzo[5,6][1,4]dithiino[2,3-*b*]thianthrene (2): To a solution of fluoro-thianthrene **(1)** (200 mg, 0.512 mmol) in nitrobenzene (10 mL) with iron powder (10 mg, 0.184 mmol) was added bromine (158.6 uL, 3.07 mmol) dropwise over 1 min. The solution was allowed to stir at 110 °C for overnight. The mixture was cooled to room temperature, mixed with diethyl ether (100 mL), and filtered. The crude off white solid was obtained (yield: 55%) and used without characterization in next step (poor solubility).

Compound (3): A toluene solution (30 mL) of tris(dibenzylideneacetone)dipalladium(0) (609.67 mg, 0.66 mmol) and *rac*-BINAP (829.08 mg, 1.33 mmol) was degassed by three freeze-pump-thaw cycles, purged with Ar, and stirred at 110 °C for 30 min. After cooling at room temperature, the mixture was added with benzophenone imine (2.75 mL, 15.98 mmol), 2,3,9,10-tetrabromo-thianthrene **2** (2 g, 2.66 mmol), and sodium *tert*-butoxide (1.54 g, 15.98 mmol), and the mixture was stirred at 110 °C overnight. The mixture was cooled at room temperature, diluted with CH_2Cl_2, filtered through a pad of Celite, and dried by rotary evaporator. The solid was pure through column chromatography on silica gel with DCM/hexane (1:2) and dried to give **3** (1.001 g, 0.90 mmol) as yellow solid in 64% yield.

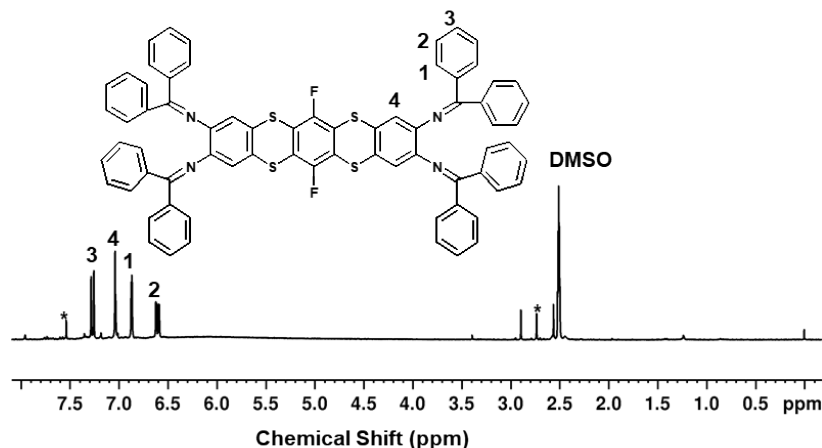^{1}H NMR (DMSO-*d*6): δ (ppm) 7.78-7.51(m, 44H, phenylene C**H**).

Figure S3. ¹H NMR spectra of **3** in DMSO at RT.

6,13-difluorobenzo[5,6][1,4]dithio[2,3-b]thianthrene-2,3,9,10-tetraamine (TATH) (4): To a THF solution (10 mL) of **3** (0.219 g, 0.17 mmol) was added a 2.0 M aqueous HCl solution (0.5 mL, 1.0 mmol) and the mixture was stirred at room temperature for 30 minutes and got precipitate (ppt). The ppt was isolated by centrifugation, washed with hexane (5.0 mL × 3), and dried under vacuum, to give (**4**) (0.02 g, 0.04 mmol) as light yellow solid in 83% yield.

¹H NMR (DMSO-*d*6): δ (ppm) 7.25(s, 4H, phenylene CH).

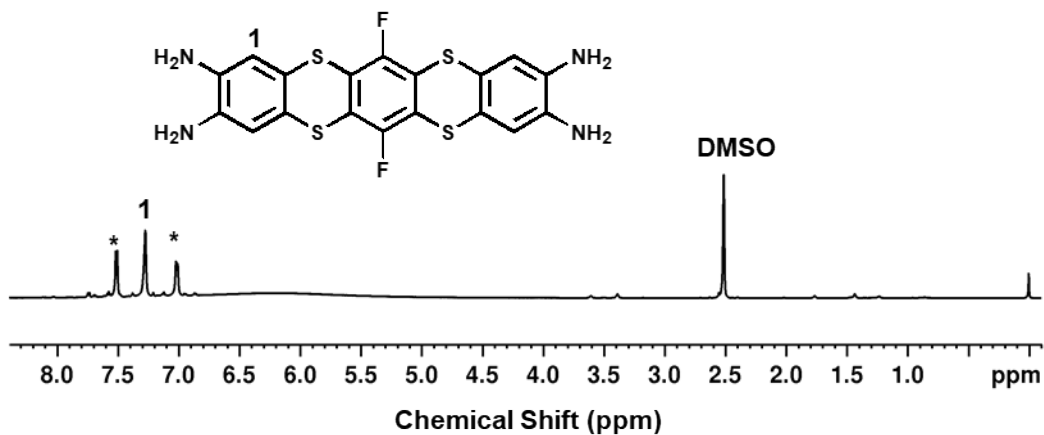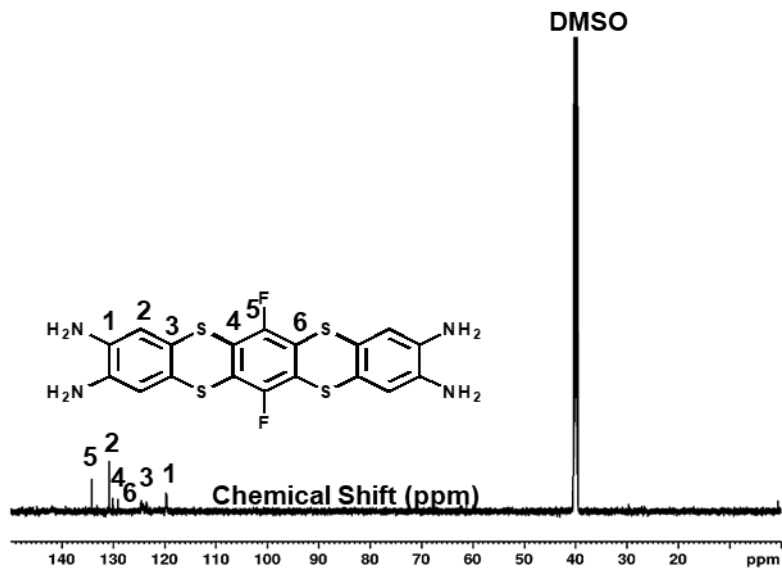Figure S4. ¹H NMR spectra of **4** in DMSO at RT.

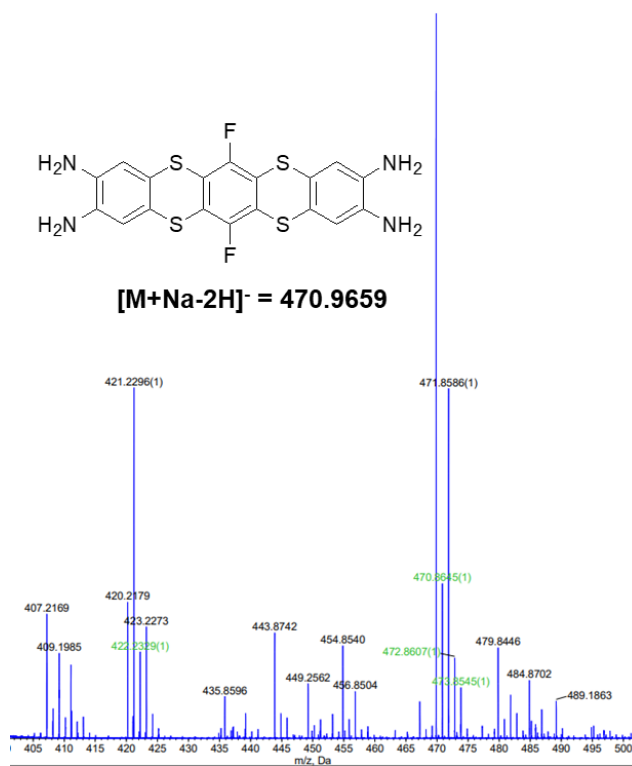Figure S5. ^{13}C NMR spectra of (**4**) in DMSO at RT.

[M+Na-2H]$^-$ = 470.9659

Figure S6. HR MS mass spectra of (**4**) in DMSO at RT.
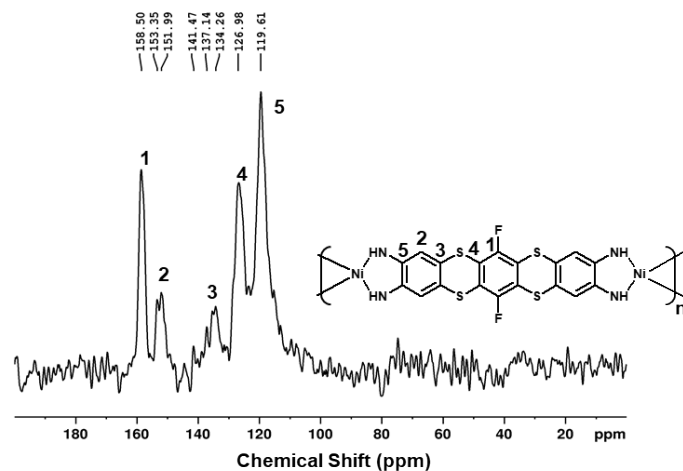
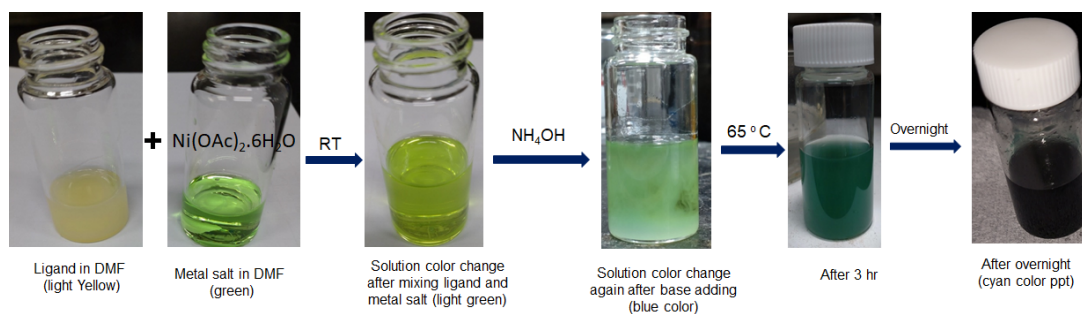Figure S7. Solid State ^{13}C NMR spectra of SKIER-5.

Figure S8. Noticeable color change during the synthesis of SKIER-5.
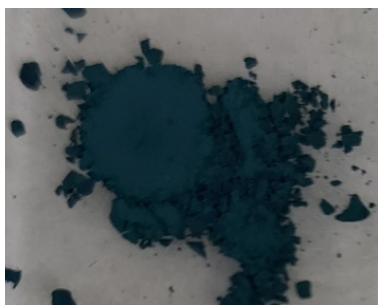

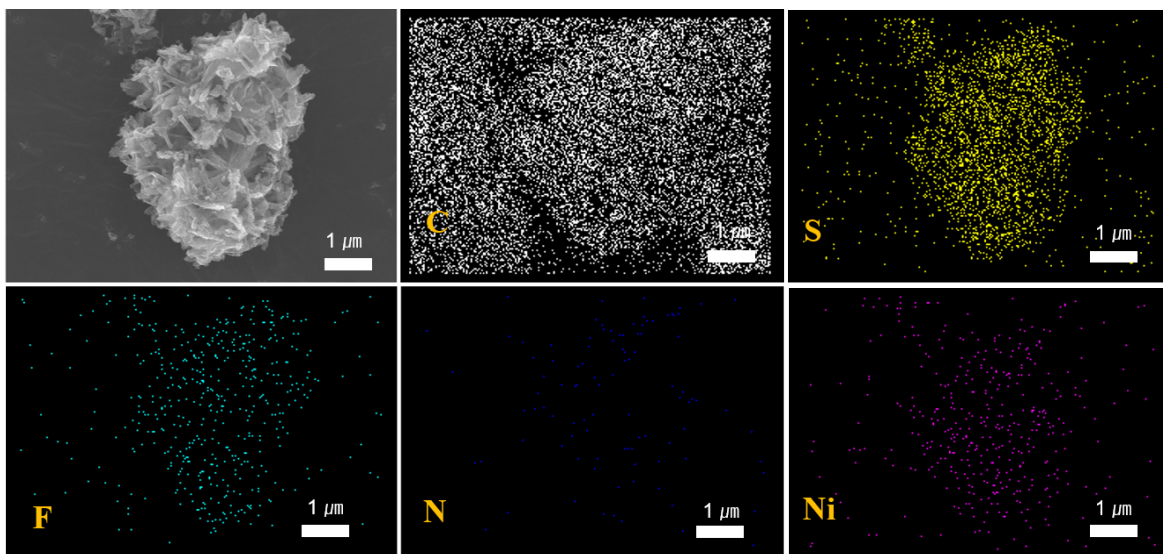Figure S9. Color image of SKIER-5 powder.
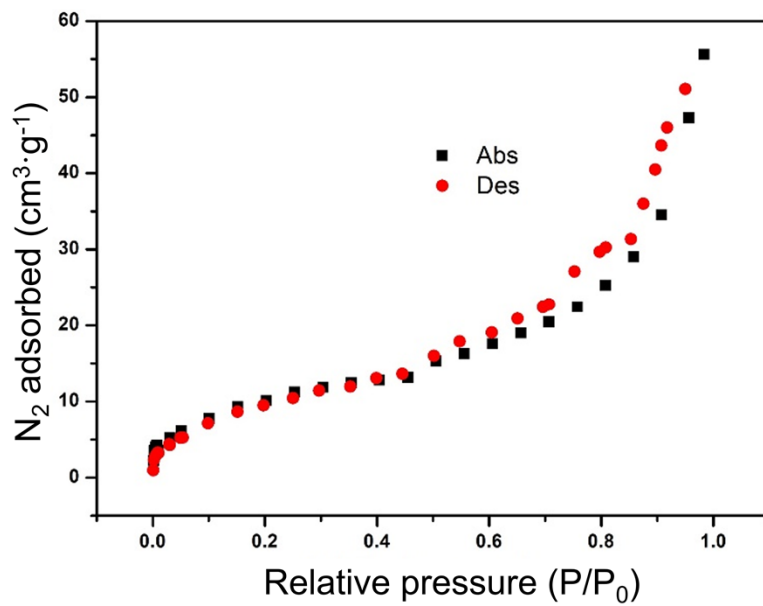
Figure S10. SEM EDS mapping of SKIER-5

Figure S11. N_2 adsorption and desorption isotherms of SKIER-5 at 77 K.
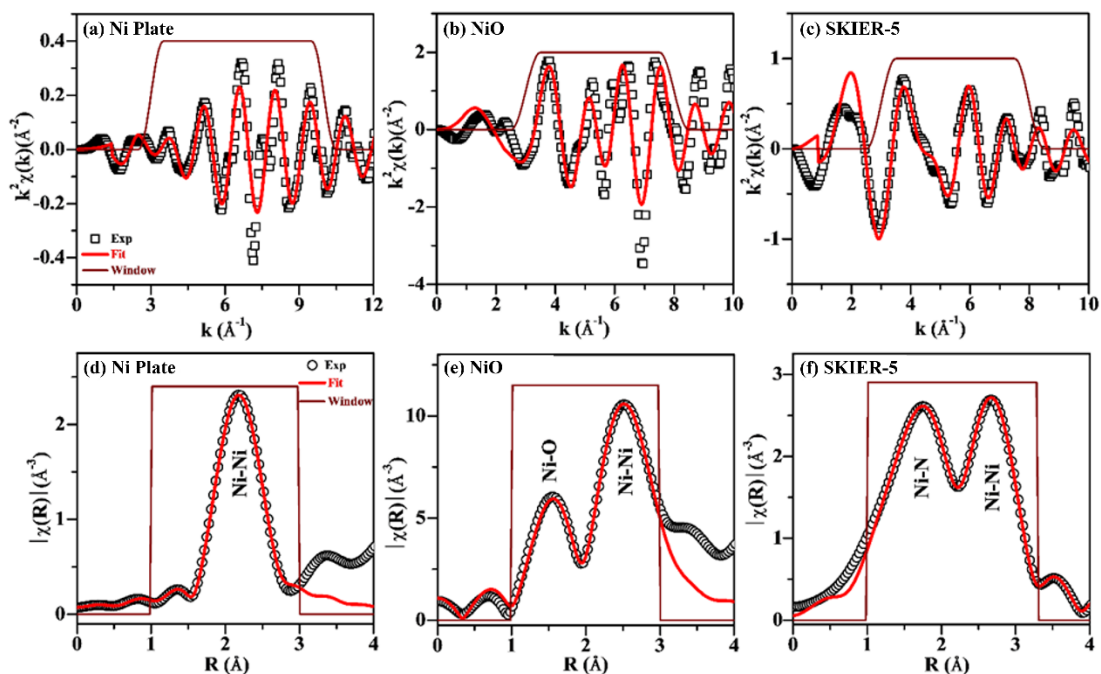
Figure S12. (a, b, c) k^2 weighted $\chi(k)$ and (d, e, f) the modulus of Fourier transform of $k^2\chi(k)$ plots of Ni K-edge EXAFS signals measured on (a, d) Ni plate, (b, e) NiO, and (c, f) SKIER-5. Open symbols, solid lines, and the window show the experimental data, fitting curve, and fitting range respectively.
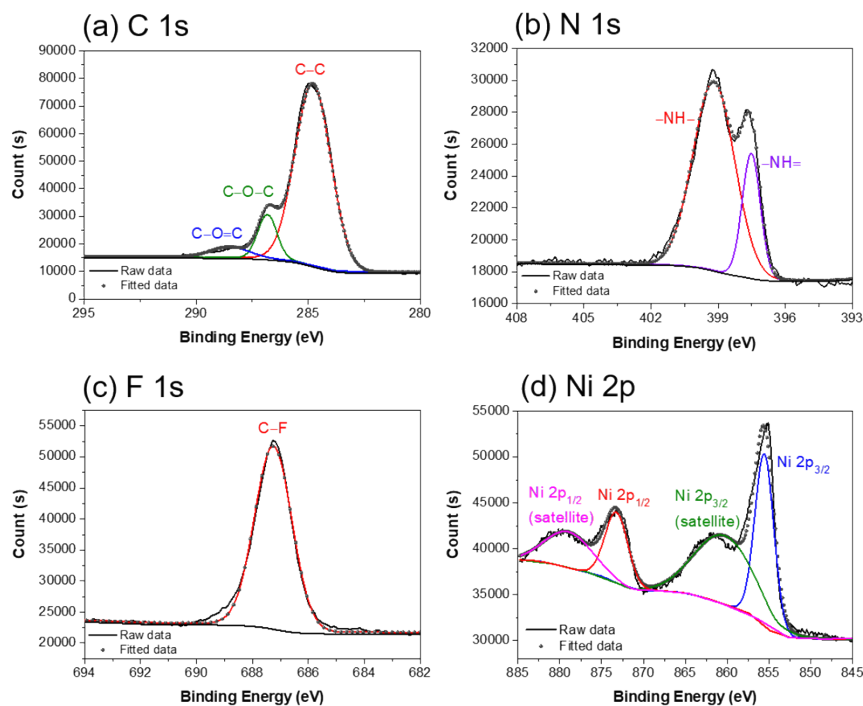

Figure S13. X-ray photoelectron spectroscopy (XPS) data deconvolution for (a) C 1s, (b) N 1s, (c) F 1s and (d) Ni 2p.

Table S1: Fitting parameters of Ni K-edge EXAFS signals such as coordination number (N), inner potential shift (ΔE_0), radial distance (R), and Debye-Waller factor (σ^2) are listed corresponding to their fitting shells for Ni plate, NiO, and SKIER-5. The goodness of fit is represented by R-factor.

Samples	Shells	N	ΔE_0 (eV)	R (Å)	σ^2 (Å^2)	R-factor
Ni plate	Ni-Ni	12.1±0.6	7.8±0.5	2.481±0.001	0.004±0.001	0.001
NiO	Ni-O	4.1±0.3	−4	2.075±0.008	0.005±0.001	0.002
SKIER-5	Ni-N	4.2±0.4	3	2.143±0.004	0.015±0.002	0.001

Table S2. Electrochemical performance of anode electrode materials for LIBs

materials	electric conductivity (S·cm^{-1})	reversible capacity	references
CuHBB	1.5×10^{-7}	90 mAh g^{-1} after 1000 cycles at 1000 mA g^{-1}	[1]
NiTIB	~10^{-8}	193 mAh g^{-1} after 40 cycles at 50 mA g^{-1}	[2]
CuTIB	~10^{-8}	98 mAh g^{-1} after 40 cycles at 50 mA g^{-1}	[3]
Ni$_3$(HITP)$_2$	1.9	703 mAh g^{-1} after 70 cycles at 50 mA g^{-1}	[4]
Cu-HHTP	1.0×10^{-2}	152.5 mAh g^{-1} after 100 cycles at 500 mA g^{-1}	[5]
Ni-HHTP	6.0×10^{-3}	910 mAh g^{-1} after 200 cycles at 100 mA g^{-1}	[6]
Ni-HAB	7.1×10^{-2}	378 F g^{-1} after 12000 cycles at 10 A g^{-1}	[7]
Co-HAB	1.57	226 mAh g^{-1} after 50 cycles at 500 mA g^{-1}	[8]
Fe$_2$(Cl$_2$dhbq)$_3$	8.4×10^{-5}	148 mAh g^{-1} after 50 cycles at 40 mA g^{-1}	[9]
Zn-PTCA	3.0×10^{-2}	302 mAh g^{-1} after 50 cycles at 200 mA g^{-1}	[10]
Cu–CAT	3.0×10^{-1}	202 F g^{-1} after 5000 cycles at 500 mA g^{-1}	[11]
SKIER-5	10^{-8}	700 mAh g^{-1} after 1600 cycles at 200 mA g^{-1}	This work

Table S3. Comparison of SKIER-5 with existing metal-organic framework-based anode materials for Li-ion storage

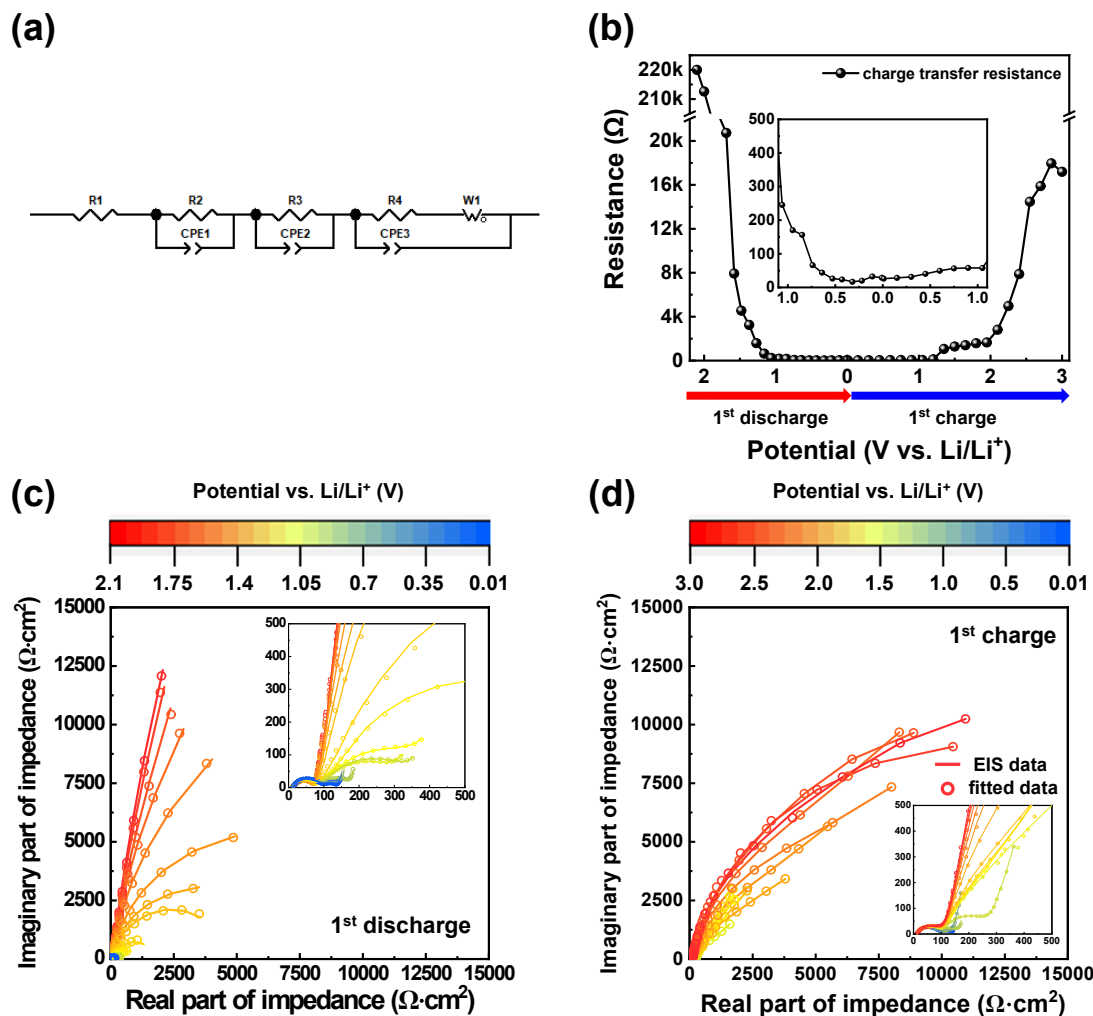| Anode Materials	Capacity (mAh g^{-1})	Discharge rate (mA g^{-1})	Potential (V vs. Li/Li$^+$)	Ref.
SKIER-5	478	113	0.01–3.00	This work
Cu-MOF	470	100	0.01–3.00	[12]
Zn(IM)$_{1.5}$(abIM)$_{0.5}$	190	100	0.01–3.00	[13]
MIL-101(Cr)	24.8	50	0.01–3.00	[14]
Mn-(tfbdc)(4,4′-bpy)(H$_2$O)$_2$	390	50	0.01–2.50	[15]
Ni-Me$_4$bpz	120	50	0.01–3.00	[16]
Ni(4,4′-bpy)(tfbdc)(H$_2$O)$_2$	406	50	0.01–3.00	[17]

Figure S14. (a) Equivalent circuit model of SKIER-5. Herein, R1 represents the bulk resistance of the SKIER-5, R2 and CPE1 represent the charge transfer resistance and constant phase element of the lithium metal. R3 and CPE2 represent the charge transfer resistance and constant phase element of the SEI layer of SKIER-5. Similarly, R4, CPE3, and W1 represent the charge transfer resistance, constant phase element, and Warburg impedance of the SKIER-5. (b) Variation of charge transfer resistance under 1st discharge/charge state, and (c, d) EIS (electrochemical impedance spectroscopy) data (lines) and fitting results (symbols) of SKIER-5.
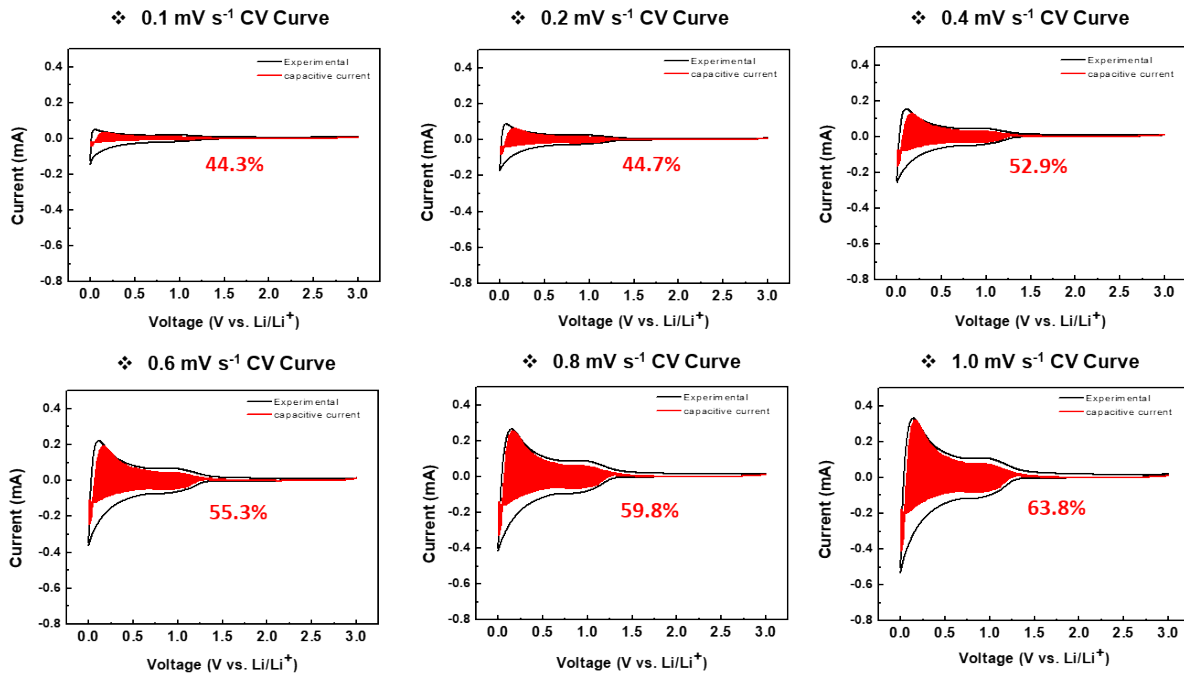
Figure S15. The capacitive contribution (red area) of SKIER-5 at the scan rates of 0.1, 0.2, 0.4, 0.6, 0.8, 1.0 mV s^{-1}.
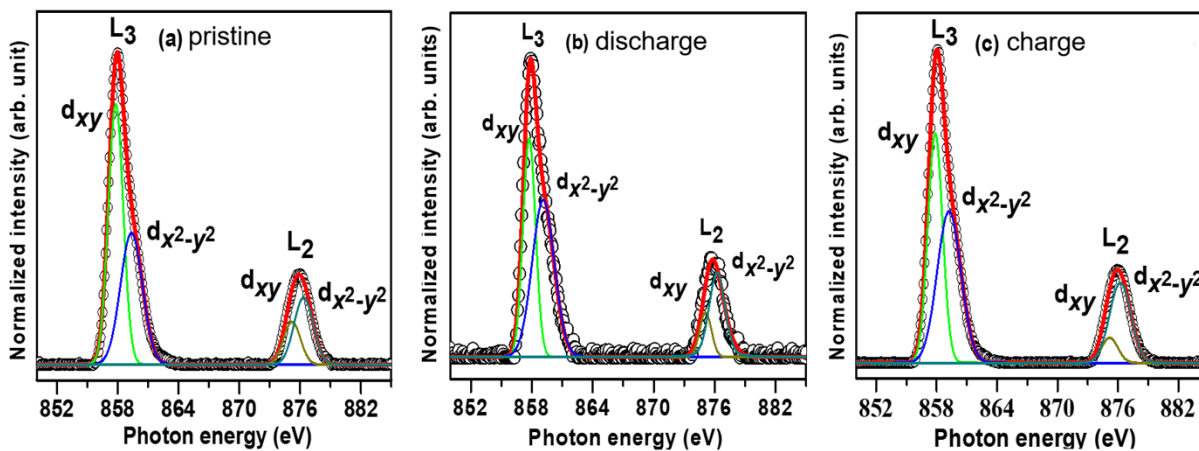

Figure S16. Ni L$_{2,3}$-edge normalized NEXAFS spectra of SKIER-5 anode after the cycle of (a) pristine, (b) 1st discharging, and (c) 1st charging.
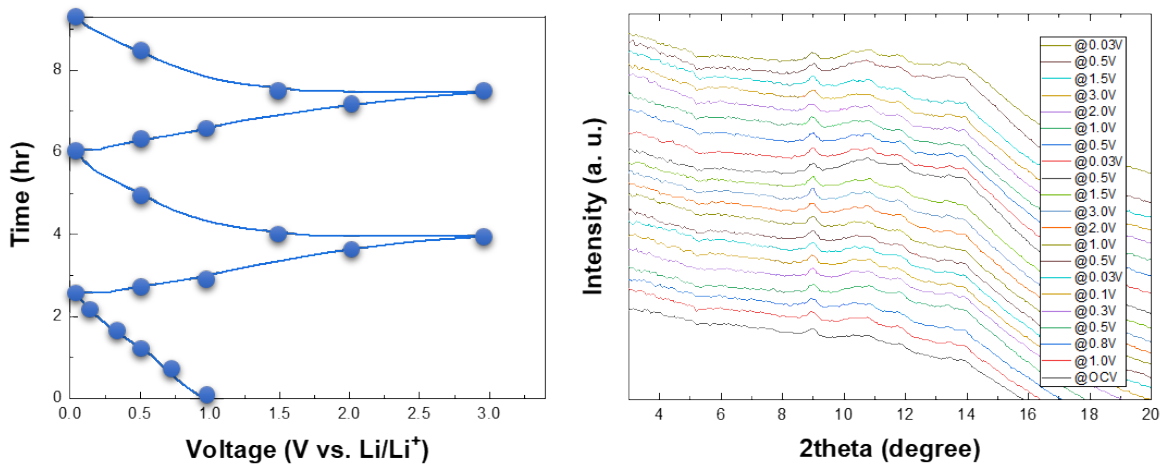
Figure S17. (anode mode) Charge-discharge graph of SKIER-5 for different cycles at 50 mA g^{-1} and in-situ PXRD profile of SKIER-5.
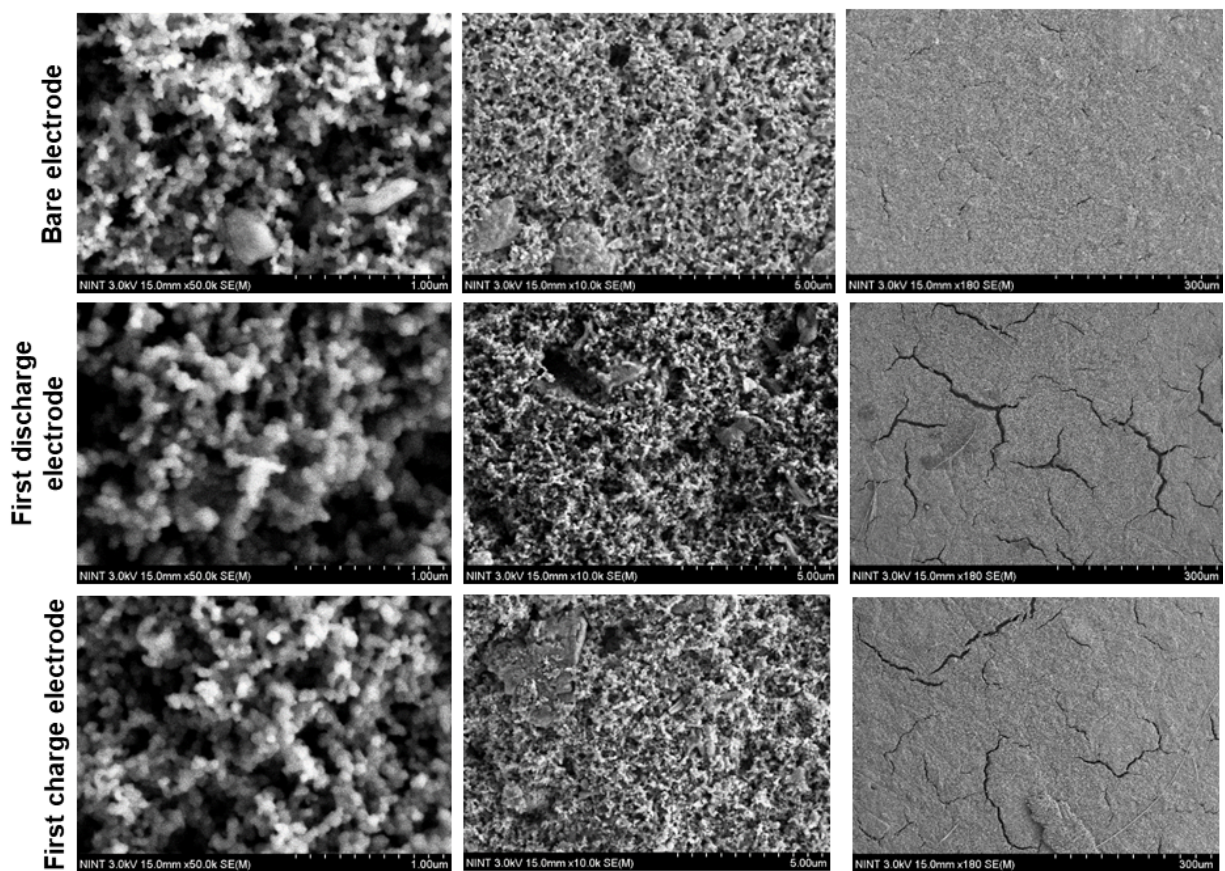

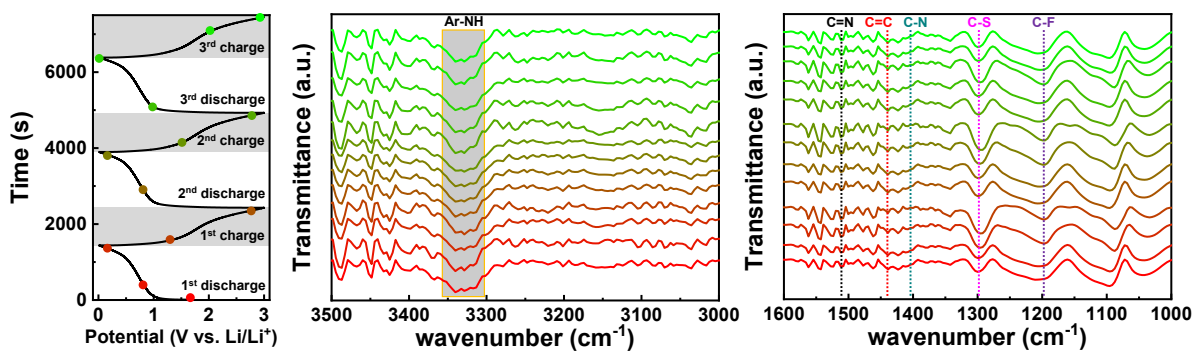Figure S18. SEM images of SKIER-5 electrodes.

Figure S19. *In-situ* FT-IR spectra of SKIER-5 at different charge/discharge states.
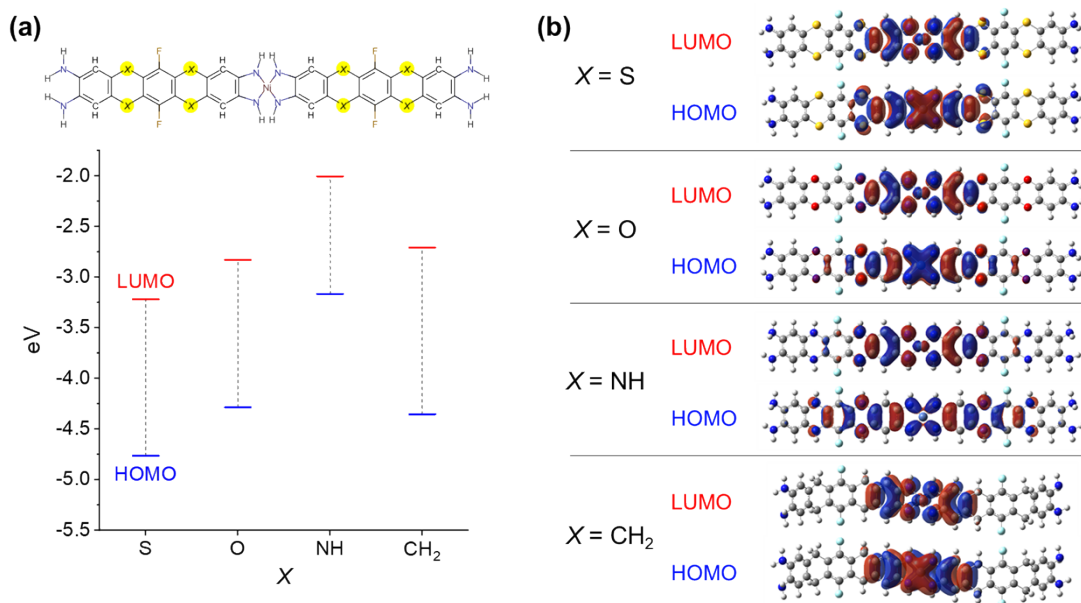
Figure S20. (a) Calculated HOMO and LUMO levels and (b) spatial distributions of non-periodic Ni(TATH) structures (X = S, O, N, C).

➢ Initial Li binding sites

① Tetra-amin site   ② Tetra-amin site   ③ S-F site   *Graphite

E_i (Li) = −1.68 eV E_i(Li) = −1.39 eV E_i(Li) = −0.72 eV E_i(Li) = −0.34 eV
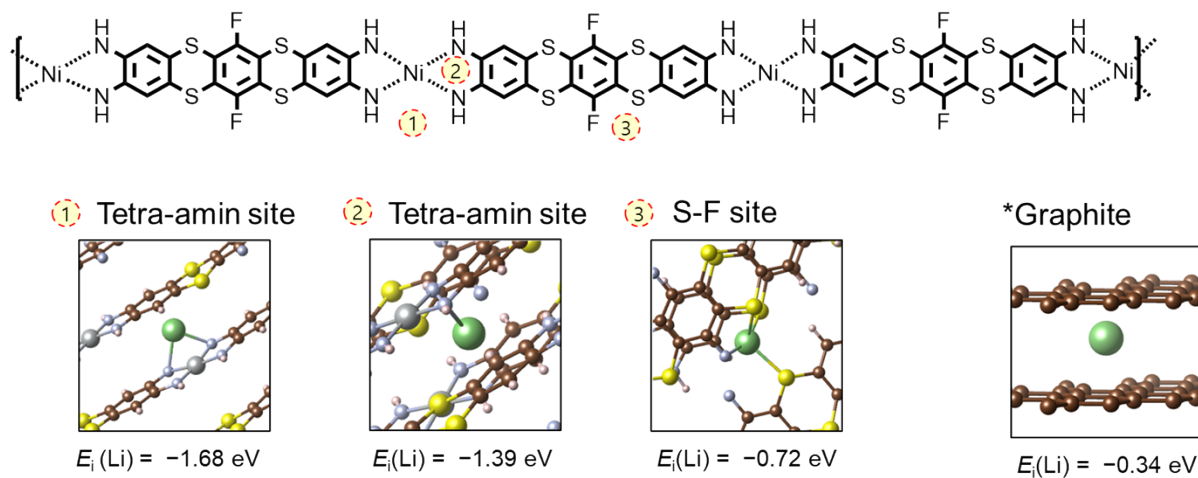
Figure S21. Single Li ion intercalation in SKIER-5: DFT-predicted sites and binding energies.
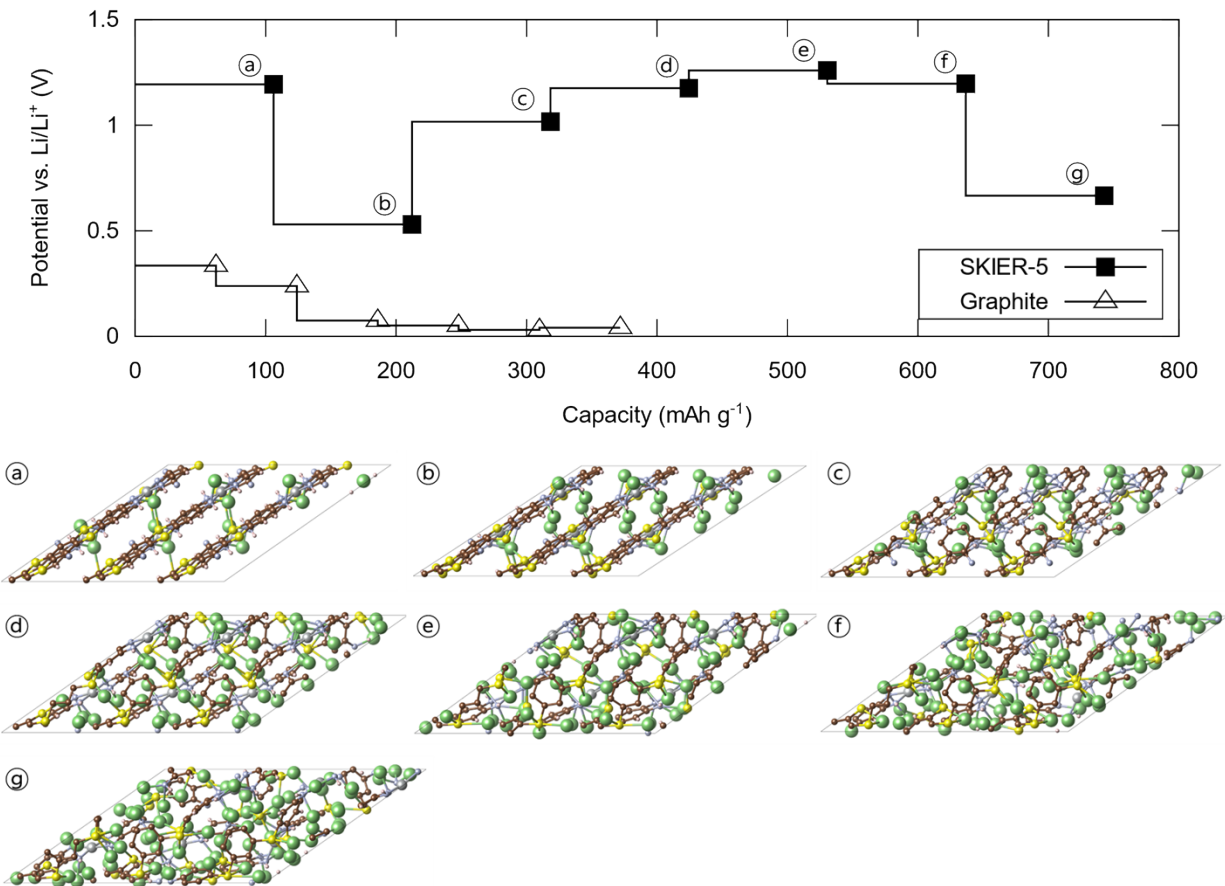
Figure S22. DFT-calculated theoretical capacity of SKIER-5 (743 mAh g^{-1}) compared with that of graphite (372 mAh g^{-1}). The optimized structures of SKIER-5 with varying Li-content corresponding to each data point are depicted below.

Figure S23. Low-temperature electrochemical performance of commercial graphite half cells at various temperatures from 25 to −20 °C. (a) Temperature-dependent galvanostatic cycling of cells at 74.4 mA g^{-1} (0.2C). (b) 5th cycle discharge–charge curves of commercial graphite.

Figure S24. Low-temperature electrochemical performance of commercial graphite with high content of Super P (50 wt%) half cells at 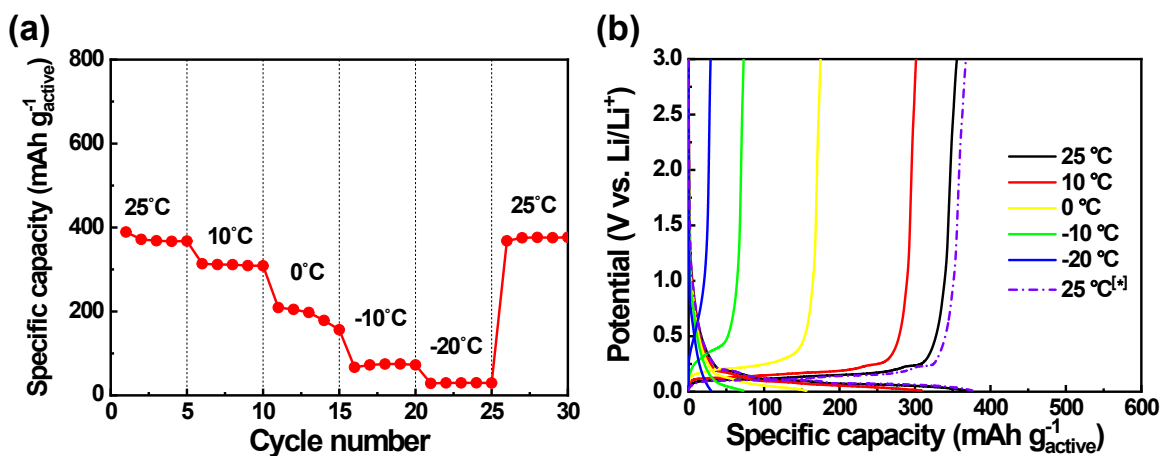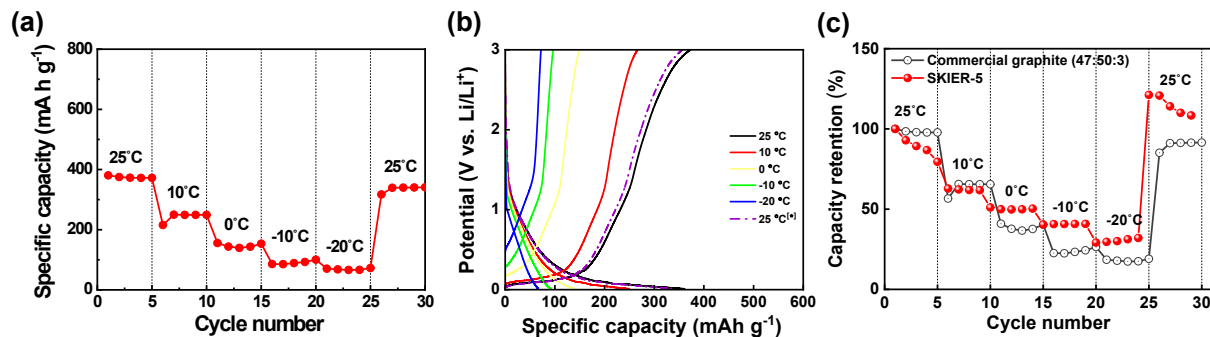various temperatures from 25 to −20 °C. (a) Temperature-dependent galvanostatic cycling of cells at 74.4 mA g^{-1} (0.2C). (b) 5th cycle discharge–charge curves of commercial graphite (c) Temperature-dependent capacity retention of commercial graphite and SKIER-5 at 74.4 mA g^{-1} (capacity retention represents the percentages of the capacity at 25 °C). Herein, the electrochemical performance was evaluated based on the total weight of the electrode.

Table S4. Comparison of the cyclic performance (mAh g^{-1}) of SKIER-5 and commercial graphite with high content of Super P (50 wt%) at 0.2C at different temperatures ranging from 25 °C to −20 °C (0.2C=113 mA g^{-1} for SKIER-5 and 0.2C=74.4 mA g^{-1} for commercial graphite)

Electrodes	Discharge capacity (mAh g^{-1}) at various temperature					
	25 ˚C	10 ˚C	0 ˚C	−10 ˚C	−20 ˚C	25 ˚C
SKIER-5	191.37[a] (100%)[b]	136.21 (71.2)	111.01 (58.0)	89.95 (47.0)	70.64 (36.9)	238.98 (124.8)
Commercial graphite	372.37 (100%)	249.10 (67.0)	153.57 (41.2)	100.53 (27.0)	66.59 (17.8)	338.33 (90.8)

[a] The electrochemical performance was evaluated based on the total weight of the electrode.
[b] The numbers in brackets represent the percentages of the capacity at 25 °C.

References

[1] Z. Wang, G. Wang, H. Qi, M. Wang, M. Wang, S. Park, H. Wang, M. Yu, U. Kaiser, A. Fery, S. Zhou, R. Dong and X. Feng, *Chemical Science,* 2020, **11**, 7665-7671.

[2] R. R. Kapaev, S. Olthof, I. S. Zhidkov, E. Z. Kurmaev, K. J. Stevenson, K. Meerholz and P. A. Troshin, *Chemistry of Materials,* 2019, **31**, 5197-5205.

[3] Y. Lian, W. Yang, C. Zhang, H. Sun, Z. Deng, W. Xu, L. Song, Z. Ouyang, Z. Wang, J. Guo, Y. Peng, *Angewandte Chemie International Edition,* 2020, **59**, 286-294 (2020).

[4] K. W. Nam, S. S. Park, R. dos Reis, V. P. Dravid, H. Kim, C. A. Mirkin and J. F. Stoddart, *Nature Communications,* 2019, **10**, 4948.

[5] S. Wang, F. Huang, Z. Zhang, W. Cai, Y. Jie, S. Wang, P. Yan, S. Jiao, R. Cao, *Journal of Energy Chemistry,* 2021, **63**, 336-343.

[6] D. Feng, T. Lei, M. R. Lukatskaya, J. Park, Z. Huang, M. Lee, L. Shaw, S. Chen, A. A. Yakovenko, A. Kulkarni, J. Xiao, K. Fredrickson, J. B. Tok, X. Zou, Y. Cui and Z. Bao, *Nature Energy,* 2018, **3**, 30-36.

[7] J. Park, M. Lee, D. Feng, Z. Huang, A. C. Hinckley, A. Yakovenko, X. Zou, Y. Cui and Z. Bao, *Journal of the American Chemical Society,* 2018, **140**, 10315-10323.

[8] M. E. Ziebel, C. A. Gaggioli, A. B. Turkiewicz, W. Ruy, L. Gagliardi and J. R. Long, *Journal of the American Chemical Society,* 2020, **142**, 2653-2664.

[9] Y. Liu, X. Zhao, C. Fang, Z. Ye, Y. He, D. Lei, J. Yang, Y. Zhang, Y. Li, Q. Liu, Y. Huang, R. Zeng, L. Kang, J. Liu, Y. Huang, *Chem,* 2018, **4**, 2463-2478.

[10] W.-H. Li, K. Ding, H.-R. Tian, M.-S. Yao, B. Nath, W.-H. Deng, Y. Wang, G. Xu, Adv. Funct. Mater, 2017, **27**, 1702067.

[11] W. J. Ong and T. M. Swager, Nat. Chemistry, 2018, **10**, 1023.

[12] Y. Zhou, M. Wu, Y. Luo, B. Pang, X. Su, M. Zhou, L. Han, New J. Chem, 2019, **43**, 1710–1715.

[13] Y. Lin, Q. Zhang, C. Zhao, H. Li, C. Kong, C. Shen, L. Chen, *Chem. Commun.,* 2015, **51**, 697–699.

[14] G. Li, F. Li, H. Yang, F. Cheng, N. Xu, W. Shi, P. Cheng, *Inorg. Chem. Commun.*, 2016, **64,** 63–66.

[15] Q. Liu, L. Yu, Y. Wang, Y. Ji, J. Horvat, M.-L. Cheng, X. Jia, G. Wang, *Inorg. Chem., 2013,* **52,** 2817–2822.

[16] T. An, Y. Wang, J. Tang, Y. Wang, L. Zhang, G. Zheng, *J. Colloid Interface Sci.,* 2015, **445**, 320–325.

[17] T C. Shi, X. Wang, Y. Gao, H. Rong, Y. Song, H.-J. Liu, Q. Liu, *J. Solid State Electrochem.,* 2017, **21,** 2415–2423.